Large-area epitaxial Mott insulating 1T-TaSe2 monolayer on GaP(111)B

Houda Koussir, Yevheniia Chernukha, Corentin Sthioul, Emmanuel Haber, Nemanja Peric, Louis Biadala, Pierre Capiod, Maxime Berthe, Isabelle Lefebvre, X. Wallart, et al.

Large-area epitaxial Mott insulating 1T-$TaSe_2$ monolayer on GaP(111)B

H. Koussir, Y. Chernukha, C. Sthioul, E. Haber, N. Peric, L. Biadala, P. Capiod, M. Berthe, I. Lefebvre, X. Wallart, B. Grandidier and P. Diener*

Univ. Lille, CNRS, Centrale Lille, Univ. Polytechnique Hauts-de-France, Junia-ISEN, UMR 8520 - IEMN, F-59000 Lille, France

E-mail: pascale.diener@junia.com

Abstract

Two dimensional Mott materials have recently been reported in the dichalcogenides family with high potential for Mottronics applications. Nevertheless, their widespread use as a single or few layers is hampered by their limited device integration resulting from their growth on graphene - a metallic substrate. Here, we report on the fabrication of 1T-$TaSe_2$ monolayers grown by molecular beam epitaxy on semiconducting gallium phosphide substrates. At the nanoscale, the charge density wave reconstruction and a Moiré pattern resulting from the monolayer interaction with the substrate are observed by scanning tunneling microscopy. The fully open gap unveiled by tunneling spectroscopy, which can be further manipulated by the proximity of a metal tip, is confirmed by transport measurements from micrometric to millimetric scales, demonstrating a robust Mott insulating phase up to 400 K.

Mott materials such as cuprates, ruthenates or nickelates exhibit an amazingly rich physics, with several competing electronic orders such as superconductivity, charge density waves (CDW) and magnetic orders.[1–3] In some of them, in particular the narrow gap Mott insulators, the Mott insulator-metal transitions can be triggered by optical and electric pulses with interesting perspectives for the micro and nanoelectronics industry.[4–7]

The benchmark dichalcogenides Mott material is 1T-TaS_2.[8] Just like other compounds of the MX_2 family (M=Nb, Ta, Mo, W ; X=S, Se, Te), TaS_2 exhibits a lamellar hexagonal structure, with strong in-plane interactions that favor the appearance of CDW orders. In particular, the 1T polytype exhibits a CDW which is commensurate with the lattice (C-CDW) below 190 K. At this threshold, a gap appears, which is generally attributed to a CDW-driven Mott transition:[9] part of the electrons are frozen by the CDW, leaving a half filled band at the Fermi energy, splitted into lower (LHB) and upper (UHB) Hubbard bands due to electronic repulsion. The correlated metal state can be recovered upon external stimuli,[10,11] but the low critical temperature limits the potential of TaS_2 for applications.

In contrast, the C-CDW survives in the selenium-based bulk compound 1T-$TaSe_2$ up to 437 K.[12] While this crystal does not develop a Mott-Hubbard band splitting because of stronger interlayer coupling than in TaS_2, an insulating behavior has been found for the surface layer and single-layer grown on bilayer graphene.[13–16] Angle resolved photoemission and scanning tunneling spectroscopy studies indicated the existence of a Mott gap up to 250 K for the surface layer[17] and up to 450 for the single-layer.[18]

Such a high temperature is essential for the development of Mottronics devices. But the

growth of 1T-$TaSe_2$ single layer on graphene, which has a much higher conductivity, hinders the study of electrical transport in the Mott crystal, calling for the use of more resistive substrates with reduced proximity effects.[19,20] Exfoliated 1T-$TaSe_2$ layers reported on an insulating SiO_2 layer has recently been obtained, giving valuable informations on the thickness dependence of the Mott gap.[21] The SiO_2 surface is however known to be prone of charge trapping with strong impact on the stability of the electrical properties.[22,23] Additionally, two keypoints must be adressed for the development of future devices. First, large $TaSe_2$ films are required, and their on-wafer process must be compatible with the microelectronics industry. Second, dichalcogenide materials, in particular 1T-$TaSe_2$, are known to get easily oxidized[24,25]. An effective in-situ encapsulation method at the end of the growth is thus mandatory.

In principle, the two-dimensional structure of 1T-$TaSe_2$ allows for a van der Waals epitaxy on passivated conventional semiconductor substrates. As a result, dichalcogenide thin films[26] and, more recently, single layers have been grown with molecular beam epitaxy (MBE) on GaAs.[27–29] Based on these achievements, we report the successful MBE growth of 1T-$TaSe_2$ monolayer on a Se-terminated GaP(111)B substrate. While electron diffraction techniques and photoemission spectroscopy indicate the growth of the 1T polytype, the $TaSe_2$/GaP heterostructure was subsequently protected with a thin Se capping layer. First, low temperature scanning tunneling microscopy (STM) performed after the sublimation of the Se cap reveals the following features: i) the expected "Star of David" (SD) superlattice caused by the C-CDW, ii) a superimposed Moiré pattern induced by the interaction of the monolayer with the GaP substrate and, iii) a Mott gap in differential conductance spectroscopy at 77 K, which vanishes when spectroscopic measurements are acquired at smaller tip-sample distances. Then, four-point probe transport measurements of 1T-$TaSe_2$ monolayers grown on semi-insulating GaP substrates and still encapsulated with a resistive Se layer show a temperature-dependent characteristic of a Mott insulator up to 400 K. 1T-$TaSe_2$ on GaP thus offers a prolific playground for low dimensionality Mott physics, CDW and Moiré related phenomena, as well as for the development of large scale Mottronic devices at ambient temperature.

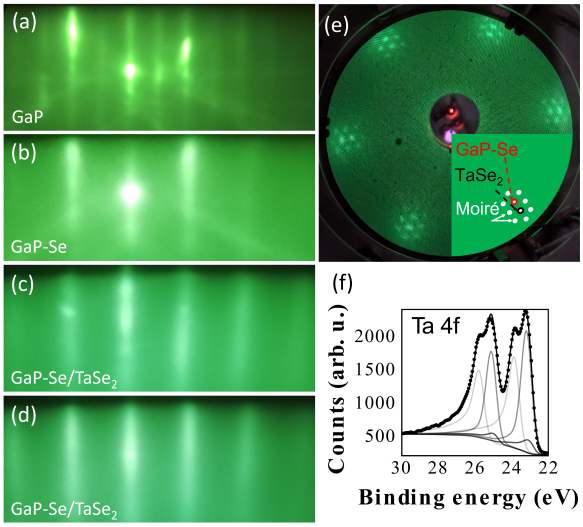

Figure 1: RHEED patterns acquired along the [11-2] azimuth for (a) the clean GaP(111)B surface, (b) the Se-treated GaP(111)B surface, (c) the growth of the $TaSe_2$ monolayer and (d) the annealed monolayer. (e) LEED pattern of the $TaSe_2$/GaP heterostructure. The diffraction spots related to the GaP, $TaSe_2$ and Moiré lattices are highlighted in red, black and white respectively. (f) XPS spectrum of Ta 4f measured with a photon energy of 1486.7 eV. The thin lines correspond to fits obtained with the parameters given in Table S1.

The growth experiments were carried out using an ultrahigh (UHV) vacuum system consisting of MBE chambers for the growth of III-V compounds and transition metal dichalcogenides. The $TaSe_2$ layer was grown at 600 °C by simultaneously supplying Ta and Se on an atomically-smooth Se-treated GaP(111)B-(1x1) surface (Figure S1). Both n-type and insulating GaP substrates have been used for the following studies. The Se passivation and growth steps were monitored by in-situ reflection high energy electron diffraction (RHEED), as shown Figures 1a-d. The observation of a streaky RHEED pattern upon the growth of the $TaSe_2$ reveals the formation of a smooth and well-ordered epilayer on the GaP substrate.

The epilayer is aligned in-plane with the substrate and becomes better ordered upon annealing at 700 °C in a Se-rich atmosphere.

The low energy electron diffraction (LEED) pattern measured at room temperature with an electron energy of 50 eV is displayed Figure 1e. The image has the expected hexagonal symmetry and the spots called "$TaSe_2$" and "GaP" are attributed to the $TaSe_2$ layer and GaP(111)B surface respectively. This pattern together with the RHEED ones show that the hexagonal cell of $TaSe_2$ aligns with that of GaP according to the relations $[0001]TaSe_2//[\bar{1}\,\bar{1}\,\bar{1}]GaP$ out of plane, $[11\bar{2}0]TaSe_2//[1\bar{1}0]GaP$ and $[1\bar{1}00]TaSe_2//[11\bar{2}]GaP$ in the plane. A Moiré pattern is visible and its analysis indicates the growth of a thin epilayer with a $(11x11)_{TaSe_2}/(10x10)_{GaP}$ structure, yielding a $TaSe_2$ lattice parameter of 3.5±0.1 Å. This value, also confirmed by X ray diffraction (Supplementary Figure S2), is close to the 1T-$TaSe_2$ bulk lattice parameter of 3.48 Å.[30] While the core level survey measured with X-ray photoelectron spectroscopy (XPS) at room temperature shows the high purity of the $TaSe_2$ layer (supplementary Figure S3), examination of the Ta 4f core level reveals a spin-orbit doubling of the 7/2 and 5/2 lines, which can be further decomposed into three components (Figure 1f). These triplets support the existence of three different Ta sites, consistent with the nonequivalent Ta atoms in the SD structure of the C-CDW phase. Moreover, the symmetry of the peaks, which differs from the asymmetry observed for the 2H-$TaSe_2$ phase, their position as well as their separation agree with previous XPS analysis of bulk 1T-$TaSe_2$ (Supplementary Table S1), further corroborating the epitaxy of the 1T-$TaSe_2$ polytype.[31]

Figure 2 displays typical STM images of a $TaSe_2$ epilayer grown on a n-type GaP substrate (doping concentration of $2\times10^{18} cm^{-3}$) after the sample transfer through air and the subsequent sublimation of the Se cap in the preparation chamber of the STM system. The large-scale image of Figure 2a shows a majority of atomic terraces with two distinct features, a quasi-periodic flower-shape pattern (evidenced by a white flower) which is superimposed to small protrusions (green triangles). These features are reproducibly observed on the whole surface, indicating the full coverage of the GaP(111)B surface with $TaSe_2$. From the height profile in Figure 2b, we measure a step height of 3.1±0.1 Å between the terraces. We note the existence of rare islands with very limited sizes, that show a height of 6.3±0.1 Å (Supplementary Figure S4). In these islands, the small protrusions are clearly visible, but the flower-shape pattern is not observed whatever the bias is. As the interlayer spacing in bulk 1T-$TaSe_2$ is 6.27 Å, the terraces cannot consist of stacked layers of 1T-$TaSe_2$. Instead, a monoatomic step height of 3.15 Å between the GaP (111) planes[32] implies that the GaP terraces are covered with a monolayer of $TaSe_2$.

Figure 2c shows a high-resolution STM image where the atoms of the top Se layer are atomically-resolved, corresponding to an atomic lattice of 3.5±0.1 Å, as expected for $TaSe_2$. The Se atoms form a bright triangular pattern rotated by an angle of 13.9° from the atomic unit cell. This pattern is at the origin of the small protrusions visible in the large scale STM image of Figure 2a. Such a superstructure is due to the SD contraction of the CDW order in the 1T phase, giving rise to a superlattice[12,15] also observed in 1T-TaS_2 and 1T-$NbSe_2$.[33,34]

Figure 3a displays a STM image at an intermediate resolution scale, in which the additional flower-shape superstructure is highlighted. The Fast Fourier Transform (FFT) of Figure 3a, shown in Figure 3b, is composed of two series of peaks, denoted P_{CDW} and P_{Moire}. Their origin is revealed by applying an inverse FFT to each series of peaks. The inverse FFT of the P_{CDW} peaks is displayed in Figure 3c, and the one corresponding to the P_{Moire} peaks, in Figure 3d. As shown in Figure 3c, the P_{CDW} peaks relates to a hexagonal lattice having a periodicity of 13.2±0.4 Å that is attributed to the SD lattice parameter. Two distinct domains are visible, having the same hexagonal lattice and rotated with respect to each other by an angle of 27.8°. As sketched Figure 3e, these domains correspond to the two equivalent chiral orientations of the SD lattice: the alignment of SDs

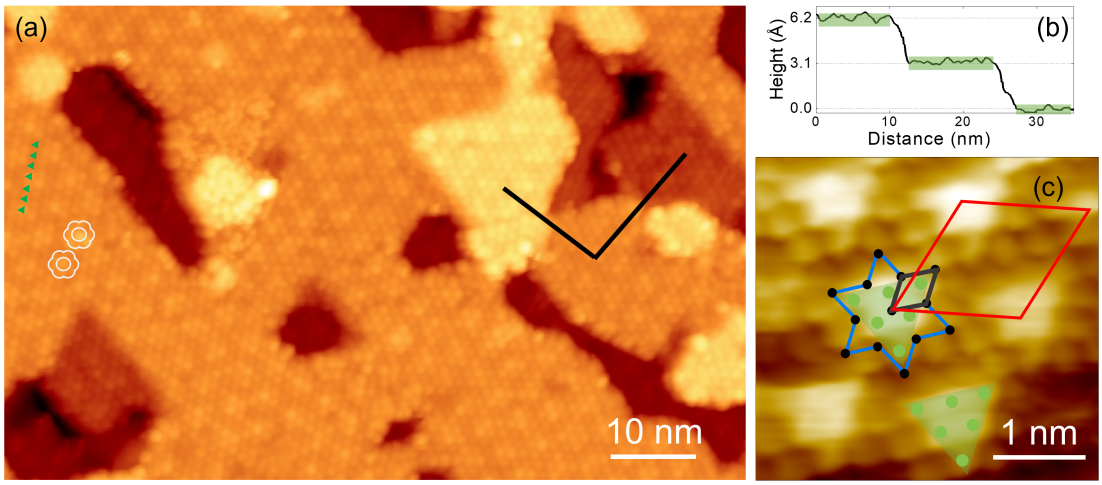

Figure 2: (a) Large scale STM image of the $TaSe_2$ monolayer. The flower-like reconstruction is highlighted in white and the CDW-related protrusions with green triangles. Feedback parameters: $V_S = +1.5$ V, $I_t = 15$ pA. (b) Height profile acquired along the black line in (a). (c) High resolution STM image where the top Se atoms of the $TaSe_2$ layer are resolved. Feedback parameters: $V_S = -0.5$ V, $I_t = 70$ pA. The Se and Ta positions are indicated by green and black atoms respectively and the CDW SD pattern by a blue star. The green triangles indicate the ensemble of top Se atoms corresponding to the small periodic protrusions in (a). The black and red diamonds delineate the atomic and CDW unit cells respectively.

on the surface can be tilted by either +13.9° or -13.9° compared to the atomic lattice.[35] Each chiral hexagonal domains give rise to 6 peaks in the FFT, rotated by approximately 28° with respect to the others.

Moreover, the P_{Moire} peaks are rotated by an angle of 14° compared to both series of P_{CDW} peaks, indicating that the Moiré pattern is aligned with the $TaSe_2$ atomic lattice. As shown in Figure 3d, the peaks P_{Moire} are related to a hexagonal lattice with a periodicity of 38.6 Å. This superlattice is consistent with a Moiré lattice formed by the superposition of the $TaSe_2$ layer and the GaP substrate, as sketched Figure 3f. In this schematic, the top atoms of the substrate (Se passivation) have a unit cell of 3.85 Å as expected for the GaP (111) surface and the $TaSe_2$ layer has a unit cell of 3.50 Å similar to the measured value. The obtained Moiré unit cell of 38.5 Å corresponds to 10 unit cells for the GaP surface and 11 $TaSe_2$ unit cells, in quantitative agreement with the Moiré observed in the LEED pattern (Figure 1e).

Surprisingly, the observed CDW lattice size of 13.2±0.4 Å is larger than the value of 12.6 Å, expected for a ($\sqrt{13} \times \sqrt{13}$ R13.9°) CDW lattice commensurable with the bulk $TaSe_2$ atomic lattice. As shown by Lin et al. in the case of $TiTe_2$ on a $PtTe_2$ substrate, a van der Waals interaction with the substrate can be at the origin of a strong modification of the CDW order present in the $TiTe_2$ monolayer.[36] The observed CDW lattice size of the $TaSe_2$ monolayer is indeed in between $\sqrt{13}a_0 = 12.6$ Å and $\sqrt{13}b_0 = 13.9$ Å with a_0 and b_0 being the in-plane $TaSe_2$ and GaP(111) lattice parameters respectively. It suggests a stretching of the CDW modulation in the $TaSe_2$ monolayer due to its proximity with the GaP substrate.

As this interaction can strongly modify the Mott gap,[36,37] tunneling spectroscopy was further performed. Figure 4a exhibits typical spectra. For feedback conditions with a large sample bias of -2.0 V, the differential conductance shows a region extending between -1.0 V and +1.3 V, where the signal is below the noise level, the Fermi level being set at zero bias. Curiously, the width of this region corresponds to the theoretical band gap of GaP at 77 K (2.26 eV). Moreover the increase of the differential conductance below -1.0 V is at odd with the dispersive bands in 1T-$TaSe_2$ monolayers grown on bilayer graphene as found in this energy range by angle-resolved photoemis-

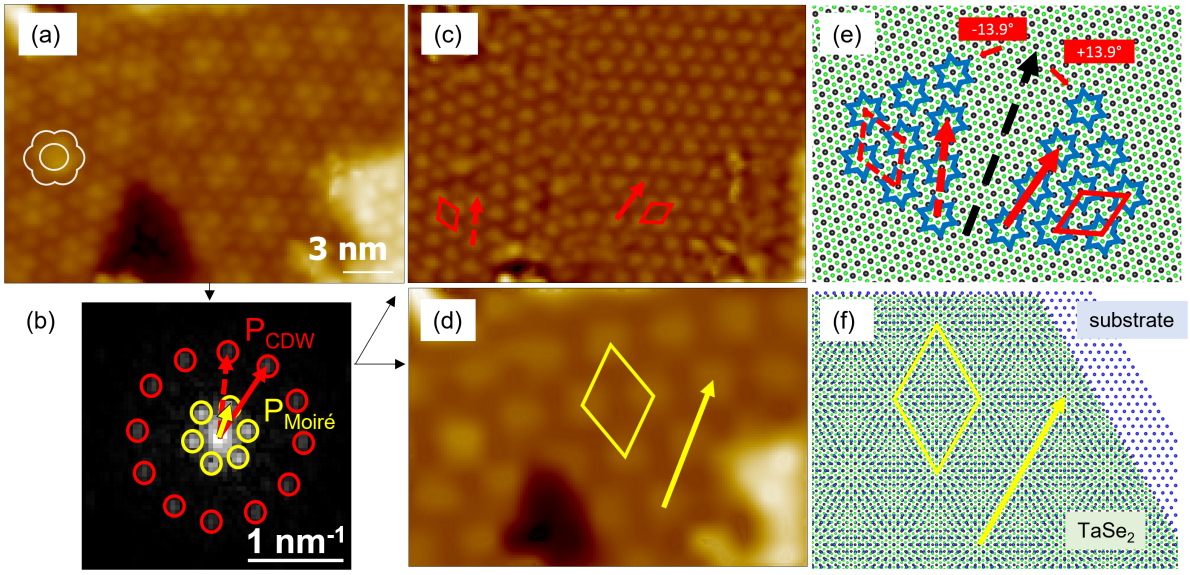

Figure 3: (a) STM image of the quasiperiodic flower-shaped superstructure observed in the 1T-$TaSe_2$ monolayer on GaP(111)B. Feedback parameters: $V_S = +3.0\,V$, $I_t = 20\,pA$. (b) FFT of image (a). The spots circled in red correspond to the CDW reconstruction and the spots circled in yellow are related to the Moiré pattern. (c,d) Inverse FFT corresponding to the CDW and the Moiré spots respectively. (e) Schematic of the two possible chiral CDW orientations. The CDW unit cell is indicated as a red diamond, either in continuous or dotted line for the two chiralities. (f) Schematic of the Moiré formed by the superposition of the Se terminated GaP substrate and the $TaSe_2$ single layer. The yellow losange gives the Moiré unit cell. The arrows in b-f underline the CDW (red) and Moiré (yellow) lattice orientations. The black and green dots in e,f are the Ta and Se atoms respectively, the blue dots in f are the atoms at the surface of the GaP substrate (Se atoms from the GaP passivation).

sion spectroscopy.[18] Therefore, we attribute the increase of the signal below -1.0 V and above +1.3 V to the contribution of the valence and conduction bands of GaP. The position of the Fermi energy 1.3 eV below the conduction band of GaP indicates a depletion layer at the surface of the n-doped substrate, consistent with the band bending deduced from photoemission measurements (Supplementary Figures S5 and S6). Noteworthy, STM images (Figure 2c) and spectroscopic measurements on the 1T-$TaSe_2$ monolayer can be still performed with sample bias within the band gap of GaP. It means that the electrons predominantly propagate through the $TaSe_2$ monolayer to reach the collecting electrode located at the sample edge, a few millimeters away from the STM tip, as illustrated by the inset of Figure 4a. Setting the feedback condition for the sample bias at -0.5 V yields a differential conductance with a zero-conductance region of $0.13 \pm 0.02\,eV$. The gap is surrounded by two peaks centered at -0.22 eV and +0.21 eV, with a Fermi energy in the middle of the gap, as expected for an undoped Mott semiconductor. The energy separation between the peaks of the LHB and UHB Hubbard bands, arising from the Coulomb repulsion in the monolayer, is 0.43 eV. The observed gap amplitude and positions of the Hubbard peaks are very similar to the one reported for 1T-$TaSe_2$ single layers on graphene bilayer,[15,38] indicating a negligible substrate perturbation and strong electronic correlations in $TaSe_2$. Based on spatially resolved tunneling spectroscopy (Figure S7), the LHB and UHB peaks are detected across the entire SD pattern. In contrast to previous results obtained at 4 K on 1T-$TaSe_2$ grown on bilayer graphene,[15] the amplitude of the UHB peak decreases at the center of the SD pattern but does not disappear. This could be attributed to a larger spatial extension of the electronic states at 77 K.

Interestingly, increasing the setpoint current causes a broadening of the LHB and UHB

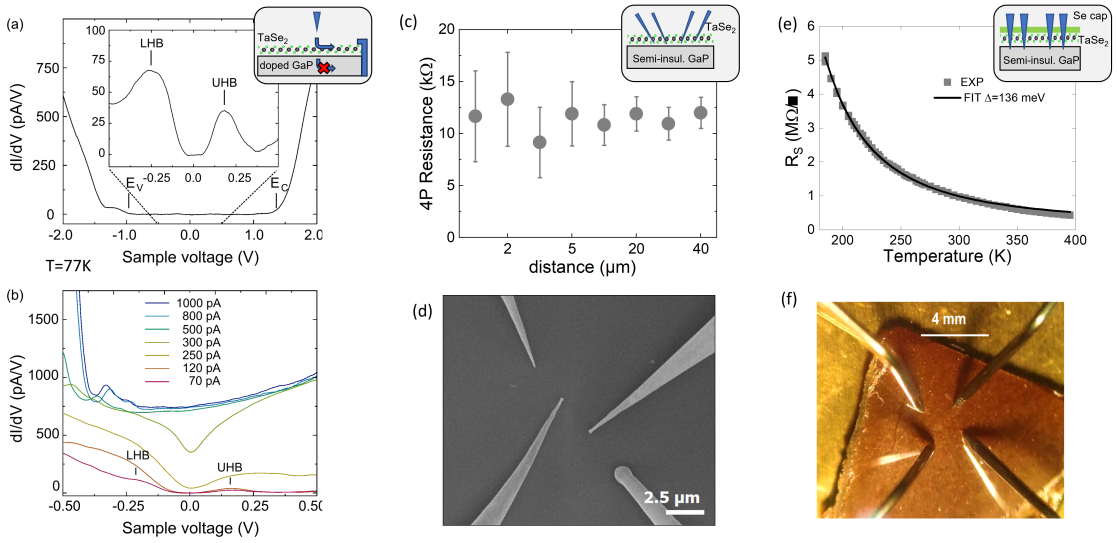

Figure 4: (a) Tunneling spectroscopy of the 1T-$TaSe_2$/GaP(111)B heterostructure. The valence and conduction band edges of the GaP substrate are indicated by vertical segments, labelled E_V and E_C. Feedback parameters: V_S = -2.0 V, I_t = 200 pA. Central inset: dI/dV spectrum acquired in a narrower energy window with different feedback parameters: V_S = -0.5 V, I_t =20 pA. The peaks related to the lower and upper Hubbard bands are respectively labelled LHB and UHB. Top inset: illustration of the measurement configuration, with the tip tunneling on the 1T-$TaSe_2$ layer grown on a doped GaP substrate. Both the $TaSe_2$ epilayer and the doped GaP substrate are in electrical contact with the ground. The arrows indicate the allowed (without cross) and forbidden (with a cross) paths for the electrons at energies below the band gap of GaP. (b) Tunneling spectroscopy performed on the same site at different setpoint currents indicated in the graph. (c) Room temperature four probe resistance as a function of the equidistant interelectrode distance measured in UHV. Inset: Illustration of the corresponding measurements configuration. (d) Scanning electron microscopy of the four aligned and equally spaced STM tips in contact with the $TaSe_2$ layer, used for (c). (e) Sheet resistance R_S as a function of temperature measured in Se-capped $TaSe_2$ (symbols) compared to the fit described in the text (line). Inset: illustration of the transport measurements configuration. The $TaSe_2$ monolayer grown on a semi-insulating GaP substrate is protected with a Se cap and the four electrodes are contacted across the cap. (f) Optical image of the sample and electrodes used in (e).

bands, which ends up with the disappearance of the Mott gap for setpoint currents higher than 250 pA (Figure 4b). In this regime, the I(V) characteristics show a metallic behavior, which strongly departs from the zero-current region measured around zero volt when the STM tip is far from the surface (Supplementary Figure S8). This result is consistent with the behavior of the Mott-Hubbard surface states of the 6H-SiC(0001), where the states do not shift but broadened upon increasing setpoint currents.[39] The increasing proximity of the metallic tip modifies the electron repulsion in the bands[40] and, hence, gives rise to a transition between the two competing phases.

To confirm the macroscopic continuity of the $TaSe_2$ monolayer, four probe transport measurements have been performed at both micrometric and millimetric scales. For these experiments, an insulating GaP substrate is used to avoid an electrical conduction through the substrate. The micrometric measurements were performed with a multiple probe STM, in UHV, at room temperature, after the sublimation of the Se cap. A linear arrangement of equidistant STM tips, as seen in the SEM image of Figure 4d, yields a 4P resistance which does not significantly vary with the tip separation (Figure 4c). Despite the roughness of the surface caused by the GaP terraces and the defects observed on each terrace, the electron conduction which is confined in the two-dimensional $TaSe_2$

monolayer, does not degrade over tens of micrometers. This is consistent with the low temperature STM experiments, where the electrons can only escape from the sample by reaching the few-millimetre-remote top contact applied to the $TaSe_2$ monolayer. This property indicates a strong robustness of transport to defects.

Temperature dependent resistance measurements have also been performed at the millimetric scale (Figure 4e-f). While the $TaSe_2$ epilayer is contacted with four golden probes through a 30 nm thick selenium cap in ambient air, the transport properties are further measured in a cryogenic setup under vacuum to avoid any degradation of the sample when it is overexposed to air. All measured current-voltage characteristics exhibit an ohmic behaviour (supplementary Figure S9), from which the temperature-dependent sheet resistance R_S is deduced for a four-probe square configuration.[41] As shown in Figure 4e, the sheet resistance R_S decreases exponentially with temperature between 200 K and 400 K. Comparison of R_S with a sample consisting of a selenium cap without the $TaSe_2$ monolayer clearly shows that the variation of R_S is caused by the intrinsic property of the 1T-$TaSe_2$ monolayer (supplementary Fig. S8). The fit with a standard activated law $R \propto exp(\Delta/2k_BT)$ gives an energy gap of Δ=136 meV. This is in remarkable agreement with the results from tunneling spectroscopy at 77 K, especially regarding the huge difference of the probed area, from the nanoscale to the milimeter scale. Such a result demonstrates that the 1T-$TaSe_2$ monolayer is in the Mott insulating state not only at low temperature, but also at room temperature.

To conclude, 1T-$TaSe_2$ epitaxial monolayers have been grown by MBE on both doped and insulating GaP substrates. The atomic superstructure observed by STM is due to a combination of a Moiré pattern with the substrate and the CDW reconstruction in both chiral orientations. A Mott insulating gap is observed both at the nanoscale by STS and millimetric scale by four point measurements, up to 400 K. The possibility to obtain similar 2D crystals on either conducting or insulating GaP substrates, with an efficient selenium encapsulation, is suitable for both lateral and transverse electrode geometry in future device applications. Besides unveiling stimulating results on the Moiré and Mott-CDW physics, the long-range electrical transport and the manipulation of the Mott gap in tunneling spectroscopy at the local scale pave the way towards the growth of large scale 2D Mott materials and their integration in functional devices at ambient temperature.

Supporting Information Experimental methods and additional experimental results.

Acknowledgement

This work was partly funded by the RENATECH network (PCMP-PCP and CMNF), I-SITE ULNE (R-20-004), Hauts-de-France region and the French National Research Agency (ANR-21-CE24-0030 Tunne2D and ANR-21-CE24-0001-01 Nanodyn).

References

(1) Lee, P. A.; Nagaosa, N.; Wen, X.-G. Doping a Mott insulator: Physics of high-temperature superconductivity. *Rev. Mod. Phys.* **2006**, *78*, 17–85.

(2) Li, D.; Lee, K.; Wang, B. Y.; Osada, M.; Crossley, S.; Lee, H. R.; Cui, Y.; Hikita, Y.; Hwang, H. Y. Superconductivity in an infinite-layer nickelate. *Nature* **2019**, *572*, 624–627.

(3) Yatsuzuka, H.; Haraguchi, Y.; Matsuo, A.; Kindo, K.; Katori, H. A. Spin-glass transition in the spin–orbit-entangled Jeff = 0 Mott insulating double-perovskite ruthenate. *Sci Rep* **2022**, *12*, 2429.

(4) Takagi, H.; Hwang, H. Y. An Emergent Change of Phase for Electronics. *Science* **2010**, *327*, 1601–1602.

(5) Basov, D. N.; Averitt, R. D.; Hsieh, D. Towards properties on demand in quantum materials. *Nat. Mater.* **2017**, *16*, 1077–1088.

(6) Pickett, M. D.; Medeiros-Ribeiro, G.; Williams, R. S. A scalable neuristor built with Mott memristors. *Nat Mater* **2013**, *12*, 114–117.

(7) Ran, Y.; Pei, Y.; Zhou, Z.; Wang, H.; Sun, Y.; Wang, Z.; Hao, M.; Zhao, J.; Chen, J.; Yan, X. A review of Mott insulator in memristors: The materials, characteristics, applications for future computing systems and neuromorphic computing. *Nano Res.* **2023**, *16*, 1165–1182.

(8) Sipos, B.; Kusmartseva, A. F.; Akrap, A.; Berger, H.; Forró, L.; Tutiš, E. From Mott state to superconductivity in 1T-TaS2. *Nature Mater* **2008**, *7*, 960–965.

(9) Ritschel, T.; Trinckauf, J.; Koepernik, K.; Büchner, B.; Zimmermann, M. v.; Berger, H.; Joe, Y. I.; Abbamonte, P.; Geck, J. Orbital textures and charge density waves in transition metal dichalcogenides. *Nature Phys* **2015**, *11*, 328–331.

(10) Stojchevska, L.; Vaskivskyi, I.; Mertelj, T.; Kusar, P.; Svetin, D.; Brazovskii, S.; Mihailovic, D. Ultrafast Switching to a Stable Hidden Quantum State in an Electronic Crystal. *Science* **2014**, *344*, 177–180.

(11) Yoshida, M.; Suzuki, R.; Zhang, Y.; Nakano, M.; Iwasa, Y. Memristive phase switching in two-dimensional 1T-TaS2 crystals. *Sci. Adv.* **2015**, *1*, e1500606.

(12) Wilson, J. A.; Di Salvo, F. J.; Mahajan, S. Charge-Density Waves in Metallic, Layered, Transition-Metal Dichalcogenides. *Phys. Rev. Lett.* **1974**, *32*, 882–885.

(13) Perfetti, L.; Georges, A.; Florens, S.; Biermann, S.; Mitrovic, S.; Berger, H.; Tomm, Y.; Höchst, H.; Grioni, M. Spectroscopic Signatures of a Bandwidth-Controlled Mott Transition at the Surface of 1T-TaSe2. *Phys. Rev. Lett.* **2003**, *90*, 166401.

(14) Nakata, Y.; Yoshizawa, T.; Sugawara, K.; Umemoto, Y.; Takahashi, T.; Sato, T. Selective Fabrication of Mott-Insulating and Metallic Monolayer TaSe2. *ACS Appl. Nano Mater.* **2018**, *1*, 1456–1460.

(15) Chen, Y. et al. Strong correlations and orbital texture in single-layer 1T-TaSe 2. *Nat. Phys.* **2020**, *16*, 218–224.

(16) Chen, Y.; Ruan, W.; Cain, J. D.; Lee, R. L.; Kahn, S.; Jia, C.; Zettl, A.; Crommie, M. F. Observation of a multitude of correlated states at the surface of bulk 1T-TaSe2 crystals. *Phys. Rev. B* **2022**, *106*, 075153.

(17) Colonna, S.; Ronci, F.; Cricenti, A.; Perfetti, L.; Berger, H.; Grioni, M. Mott Phase at the Surface of 1T-TaSe2 Observed by Scanning Tunneling Microscopy. *Phys. Rev. Lett.* **2005**, *94*, 036405.

(18) Nakata, Y.; Sugawara, K.; Chainani, A.; Oka, H.; Bao, C.; Zhou, S.; Chuang, P.-Y.; Cheng, C.-M.; Kawakami, T.; Saruta, Y.; Fukumura, T.; Zhou, S.; Takahashi, T.; Sato, T. Robust charge-density wave strengthened by electron correlations in monolayer 1T-TaSe2 and 1T-NbSe2. *Nat Commun* **2021**, *12*, 5873.

(19) Chen, Y.; Wu, L.; Xu, H.; Cong, C.; Li, S.; Feng, S.; Zhang, H.; Zou, C.; Shang, J.; Yang, S. A.; Loh, K. P.; Huang, W.; Yu, T. Visualizing the Anomalous Charge Density Wave States in Graphene/NbSe2 Heterostructures. *Advanced Materials* **2020**, *32*, 2003746.

(20) Dreher, P.; Wan, W.; Chikina, A.; Bianchi, M.; Guo, H.; Harsh, R.; Mañas-Valero, S.; Coronado, E.; Martínez-Galera, A. J.; Hofmann, P.; Miwa, J. A.;

Ugeda, M. M. Proximity Effects on the Charge Density Wave Order and Superconductivity in Single-Layer NbSe2. *ACS Nano* **2021**, *15*, 19430–19438.

(21) Tian, N. et al. Dimensionality-driven metal to Mott insulator transition in two-dimensional 1T-TaSe2. *National Science Review* **2023**, nwad144.

(22) Illarionov, Y. Y.; Rzepa, G.; Waltl, M.; Knobloch, T.; Grill, A.; Furchi, M. M.; Mueller, T.; Grasser, T. The role of charge trapping in MoS2/SiO2 and MoS2/hBN field-effect transistors. *2D Mater.* **2016**, *3*, 035004.

(23) Illarionov, Y. Y.; Knobloch, T.; Jech, M.; Lanza, M.; Akinwande, D.; Vexler, M. I.; Mueller, T.; Lemme, M. C.; Fiori, G.; Schwierz, F.; Grasser, T. Insulators for 2D nanoelectronics: the gap to bridge. *Nat Commun* **2020**, *11*, 3385.

(24) Tsai, H.-S.; Liu, F.-W.; Liou, J.-W.; Chi, C.-C.; Tang, S.-Y.; Wang, C.; Ouyang, H.; Chueh, Y.-L.; Liu, C.; Zhou, S.; Woon, W.-Y. Direct Synthesis of Large-Scale Multilayer TaSe2 on SiO2/Si Using Ion Beam Technology. *ACS Omega* **2019**, *4*, 17536–17541.

(25) Samnakay, R.; Wickramaratne, D.; Pope, T. R.; Lake, R. K.; Salguero, T. T.; Balandin, A. A. Zone-Folded Phonons and the Commensurate-Incommensurate Charge-Density-Wave Transition in 1T-TaSe2 Thin Films. *Nano Lett* **2015**, *15*, 2965–2973.

(26) Tsoutsou, D.; Aretouli, K. E.; Tsipas, P.; Marquez-Velasco, J.; Xenogiannopoulou, E.; Kelaidis, N.; Aminalragia Giamini, S.; Dimoulas, A. Epitaxial 2D MoSe2 (HfSe2) Semiconductor/2D TaSe2 Metal van der Waals Heterostructures. *ACS Appl. Mater. Interfaces* **2016**, *8*, 1836–1841.

(27) Chen, M.-W.; Ovchinnikov, D.; Lazar, S.; Pizzochero, M.; Whitwick, M. B.; Surrente, A.; Baranowski, M.; Sanchez, O. L.; Gillet, P.; Plochocka, P.; Yazyev, O. V.; Kis, A. Highly Oriented Atomically Thin Ambipolar MoSe2 Grown by Molecular Beam Epitaxy. *ACS Nano* **2017**, *11*, 6355–6361.

(28) Ohtake, A.; Sakuma, Y. Two-Dimensional WSe2/MoSe2 Heterostructures Grown by Molecular-Beam Epitaxy. *J. Phys. Chem. C* **2021**, *125*, 11257–11261.

(29) Pierucci, D.; Mahmoudi, A.; Silly, M.; Bisti, F.; Oehler, F.; Patriarche, G.; Bonell, F.; Marty, A.; Vergnaud, C.; Jamet, M.; Boukari, H.; Lhuillier, E.; Pala, M.; Ouerghi, A. Evidence for highly p-type doping and type II band alignment in large scale monolayer WSe2/Se-terminated GaAs heterojunction grown by molecular beam epitaxy. *Nanoscale* **2022**, *14*, 5859–5868.

(30) Bjerkelund, E.; Kjekshus, A.; Nilsson, A.; Sandstron, J.; Theorell, H.; Blinc, R.; Pausak, S.; Ehrenberg, L.; Dumanovic, J. On the Structural Properties of the Ta1xSe2 Phase. *Acta Chem. Scand.* **1967**, *21*, 513–526.

(31) Horiba, K.; Ono, K.; Oh, J. H.; Kihara, T.; Nakazono, S.; Oshima, M.; Shiino, O.; Yeom, H. W.; Kakizaki, A.; Aiura, Y. Charge-density wave and three-dimensional Fermi surface in 1T-TaSe2 studied by photoemission spectroscopy. *Phys. Rev. B* **2002**, *66*, 073106.

(32) Hattori, K.; Ishihara, K.; Miyatake, Y.; Matsui, F.; Takeda, S.; Daimon, H.; Komori, F. GaP(111)reconstructed surface studied with STM and LEED. *Surface Science* **2003**, *525*, 57–65.

(33) Wu, Z.; Bu, K.; Zhang, W.; Fei, Y.; Zheng, Y.; Gao, J.; Luo, X.; Liu, Z.; Sun, Y.-P.; Yin, Y. Effect of stacking order on the electronic state of 1T-TaS2. *Phys. Rev. B* **2022**, *105*, 035109.

(34) Liu, L. et al. Direct identification of Mott Hubbard band pattern beyond charge den-

sity wave superlattice in monolayer 1T-NbSe2. *Nat Commun* **2021**, *12*, 1978.

(35) Song, X. et al. Atomic-scale visualization of chiral charge density wave superlattices and their reversible switching. *Nat Commun* **2022**, *13*, 1843.

(36) Lin, M.-K.; Hlevyack, J.; Chen, P.; Liu, R.-Y.; Mo, S.-K.; Chiang, T.-C. Charge Instability in Single-Layer TiTe2 Mediated by van der Waals Bonding to Substrates. *Phys. Rev. Lett.* **2020**, *125*, 176405.

(37) Zhang, W.; Wu, Z.; Bu, K.; Fei, Y.; Zheng, Y.; Gao, J.; Luo, X.; Liu, Z.; Sun, Y.-P.; Yin, Y. Reconciling the bulk metallic and surface insulating state in 1T-TaSe2. *Phys. Rev. B* **2022**, *105*, 035110.

(38) Lin, H.; Huang, W.; Zhao, K.; Qiao, S.; Liu, Z.; Wu, J.; Chen, X.; Ji, S.-H. Scanning tunneling spectroscopic study of monolayer 1T-TaS2 and 1T-TaSe2. *Nano Res.* **2020**, *13*, 133–137.

(39) Baffou, G.; Mayne, A. J.; Comtet, G.; Dujardin, G. State selective electron transport through electronic surface states of 6H-SiC(0001)-3x3. *Phys. Rev. B* **2008**, *77*, 165320, Publisher: American Physical Society.

(40) Nguyen, T. H.; Mahieu, G.; Berthe, M.; Grandidier, B.; Delerue, C.; Stiévenard, D.; Ebert, P. Coulomb Energy Determination of a Single Si Dangling Bond. *Phys. Rev. Lett.* **2010**, *105*, 226404, Publisher: American Physical Society.

(41) Miccoli, I.; Edler, F.; Pfnür, H.; Tegenkamp, C. The 100th anniversary of the four-point probe technique: the role of probe geometries in isotropic and anisotropic systems. *J. Phys.: Condens. Matter* **2015**, *27*, 223201.

Supplementary Information - Large-area epitaxial Mott insulating monolayer 1T-$TaSe_2$ on GaP(111)B

H. Koussir, Y. Chernukha, C. Sthioul, E. Haber, N. Peric, L. Biadala, P. Capiod, M. Berthe, I. Lefebvre, X. Wallart, B. Grandidier and P. Diener*

Univ. Lille, CNRS, Centrale Lille, Univ. Polytechnique Hauts-de-France, Junia-ISEN, UMR 8520 - IEMN, F-59000 Lille, France

E-mail: pascale.diener@junia.com

Epitaxial growth

The GaP(111)B substrates were deoxidized in a III-V MBE reactor under cracked phosphine (PH3) and atomic hydrogen (Hat) fluxes to prepare clean GaP(111)B surfaces. After deoxidization, the surface exhibited a 2x2 RHEED pattern and a morphology characterized by atomic steps whereas XPS revealed the absence of residual contamination.

The sample was then transferred under UHV in a TMD epitaxial chamber and annealed up to 600°C under a selenium flux with a Beam Equivalent Pressure in the 10^{-6} Torr range to prepare a Se-terminated GaP(111) surface. During selenium passivation, the RHEED pattern turned to a 1x1 reconstruction. Atomic Force Microscopy (AFM) did not reveal any surface morphology change after selenium treatment. The $TaSe_2$ growth was performed at 600°C with a Ta growth rate around 0.0015 Å/s and under a selenium beam equivalent pressure of 4-5 10^{-6} Torr. After growth, the layer was annealed for 10 minutes at 700°C.

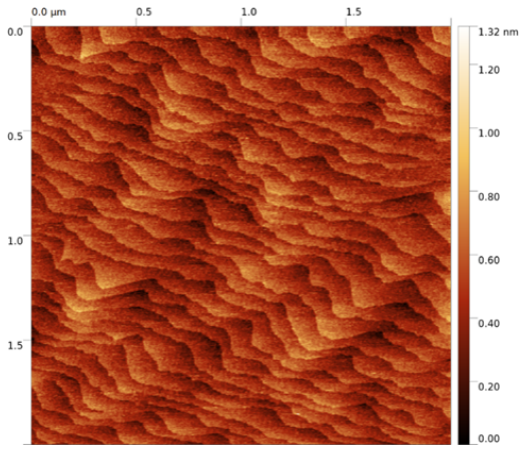

Figure S 1: 2x2 µm typical AFM image of the GaP(111)B surface after deoxidation.

Grazing Incidence X-ray Diffraction

In plane XRD measurement have been performed using a Rigaku SmartLab diffractometer at incidence 0.5° using Cu Kα1 = 1.5406 Å and Kα2 = 1.5444 Å X-rays collimated with 0.114° slits. The diffraction patterns figure S2a confirms the alignment of the $TaSe_2$ lattice on the substrate and figure S2b shows that the position of the (110) peak of $TaSe_2$ is 52.5°±0.6° which corresponds to a lattice parameter of 3.48±0.04 Å.

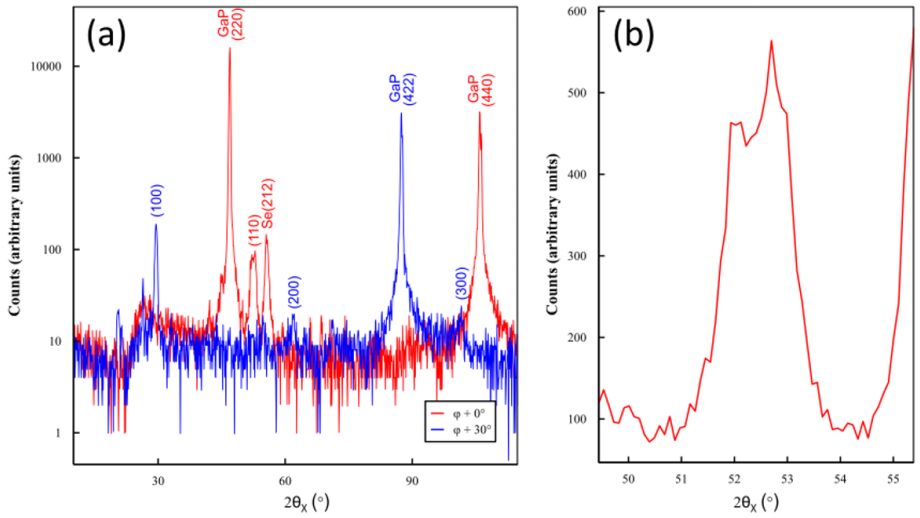

Figure S 2: (a) Large $2\theta\chi/\phi$ scan of $TaSe_2$ along the [110] and [-211] crystal directions of GaP. (b) $2\theta\chi/\phi$ Scan on a reduced range around the (110) peak of $TaSe_2$.

XPS analysis

As the ESCA analysis chamber is connected to the MBE chambers, the samples do not suffer from transfer contamination prior to their characterization by XPS. The XPS spectra have been recorded using Al Kα = 1486 eV. The high purity of the sample is confirmed by a survey in which only Ta, Se, Ga and P lines are detected.

The Ta 4f XPS core level has been fitted using the software CasaXPS[1] with Doniach-Sunjic-Shirley (DSS) line shapes.[2] They consist in Doniach-Sunjic functions,[3] the only theoretically based asymmetric curves, with a cut off to avoid their area to be infinite. This approach has already been used in 2H-$TaSe_2$ and 1T-TaS_2.[4,5] The DSS line shapes are based on Lorentzian functions which have been convoluted with a Gaussian function to reproduce the experimental broadening of the system.

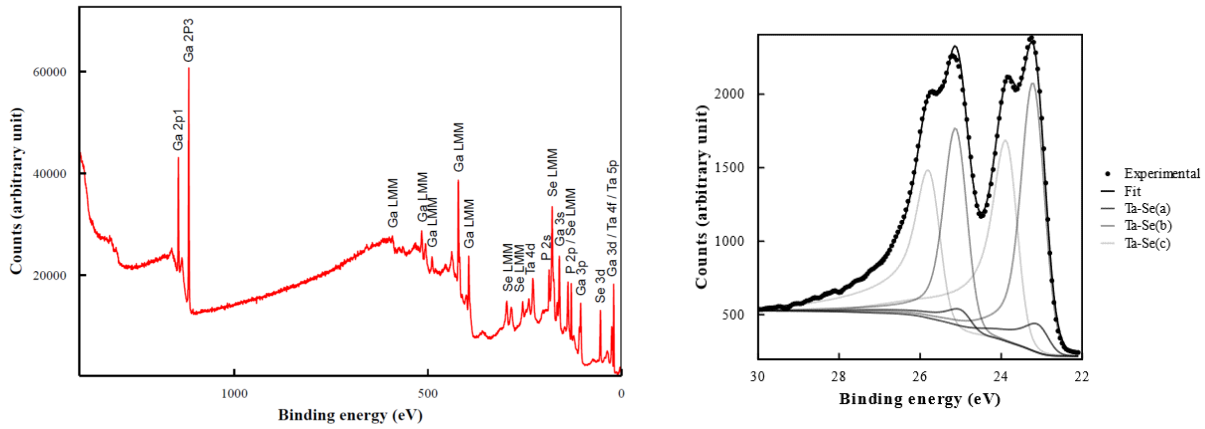

Figure S 3: Top: XPS survey of 1T-$TaSe_2$ on GaP(111)B. Bottom: Ta 4f core level spectrum. The thin lines correspond to fits obtained with the parameters given in Table S1.

The fit is made with 3 doublets corresponding to the 3 inequivalent Ta atoms in the CDW in the proportion 6:6:1, each having different asymmetries, and based on the relative peak positions from the literature.[6] The fitting parameters are as given in Table S1.

Table S 1: Fitting parameters for the Ta 4f core level in monolayer 1T-$TaSe_2$ measured by XPS. For all fits, the value of the full width at half maximum is constrained at 0.66 eV.

Bond	Area (percent)	Asymmetry parameter	Binding energy (eV)
Ta-Se(a)7/2	4.4	0.49	22.99
Ta-Se(a)5/2	3.3	0.49	24.90
Ta-Se(b)7/2	26.4	0.12	23.19
Ta-Se(b)5/2	19.7	0.12	25.10
Ta-Se(c)7/2	26.4	0.34	23.80
Ta-Se(c)5/2	19.7	0.34	25.71

Scanning Tunneling Microscopy

Scanning tunneling microscopy has been performed at 77K with a low temperature LT-Omicron setup. To be able to study the $TaSe_2$ epilayer at low temperature, the GaP substrate was n-type doped at a concentration of 2-3$\times 10^{18}$ cm^{-3}. We used electrochemically etched tungsten tips, which were thoroughly cleaned in-situ by direct current heating. Prior to the STM study, the samples were bakeout in the load lock of the system at 120°C for 8 hours. Then, the protective Se layer was removed in the preparation chamber by heating the samples at 270°C for several hours.

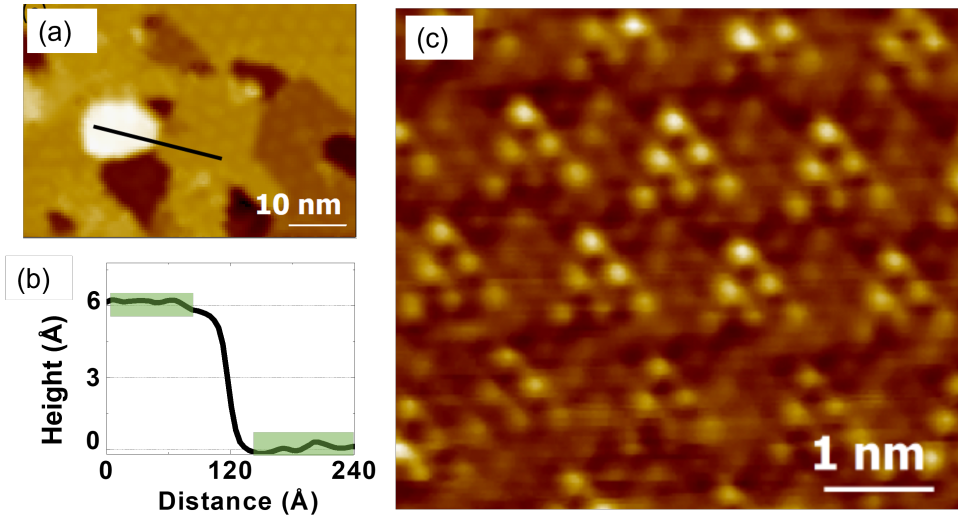

Figure S 4: (a) Typical STM image of a supposed bilayer nanosheet. (b) Height profile acquired along the segment seen in (a). (c) High resolution STM image of the bilayer (V_{sample} = -2 V ; I_t = 20 pA).

Evaluation of band-bending

We use X-ray and UV photoemission measurements to determine the surface band bending during surface passivation and upon 1 monolayer (ML) $TaSe_2$ deposition. The doping level of the sample (2-3 $10^{18}/cm^3$) and the GaP band gap (2.26 eV) allow to determine the position of the valence band maximum in the bulk E_vb with respect to the Fermi level : E_f – E_vb = 2.2 eV.

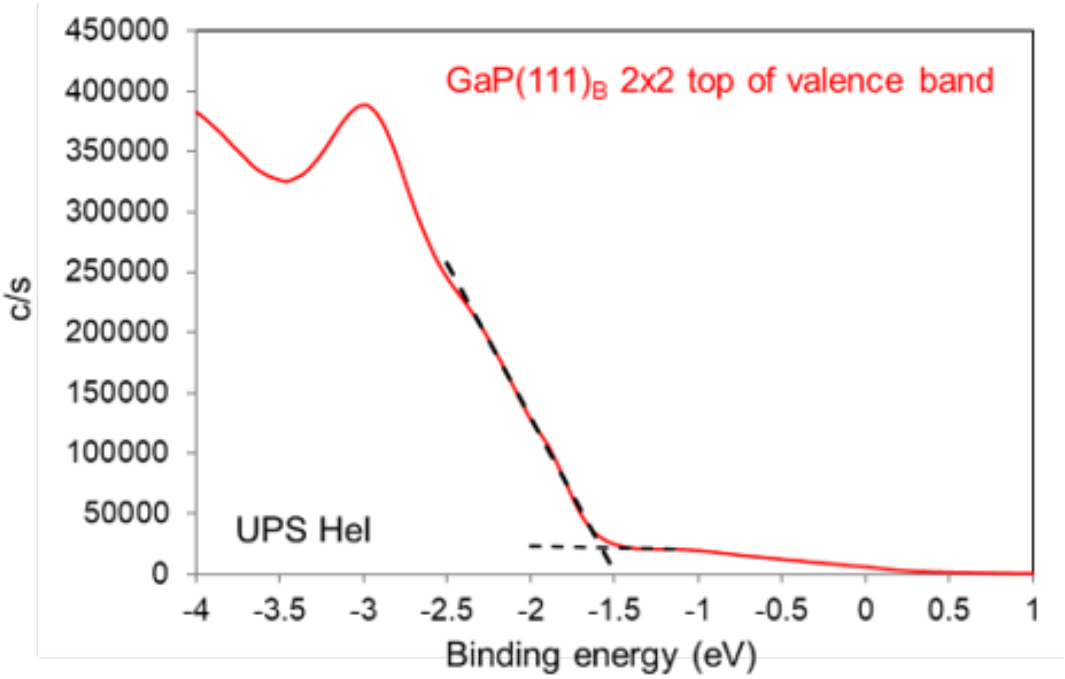

Figure S 5: Determination of the valence band maximum on the deoxidized GaP(111)B 2×2 surface.

Then, on the deoxidized n-type GaP(111)B 2×2 surface, we record the position of the valence band maximum at the surface E_{vs} with respect to the Fermi level E_f (Figure S5) by a standard linear extrapolation method.[7] This leads to E_f - E_{vs} = 1.58 eV±0.05 eV. The band bending on the deoxidized GaP(111)B 2×2 surface is then defined as E_{vs} – E_{vb} = 0.62 eV±0.05 eV. For this surface, we also record the binding energy (BE) of the P2p core level (CL) line at -129.78 eV±0.025 eV (red curve on figure S6)

During the Se surface passivation and 1 ML $TaSe_2$ deposition, we then follow the evolution of the band bending according to the variations of the BE of the P2p CL line, as the edge of

the valence band for the GaP surface might become difficult to detect upon the formation of the 1T-$TaSe_2$ epilayer.

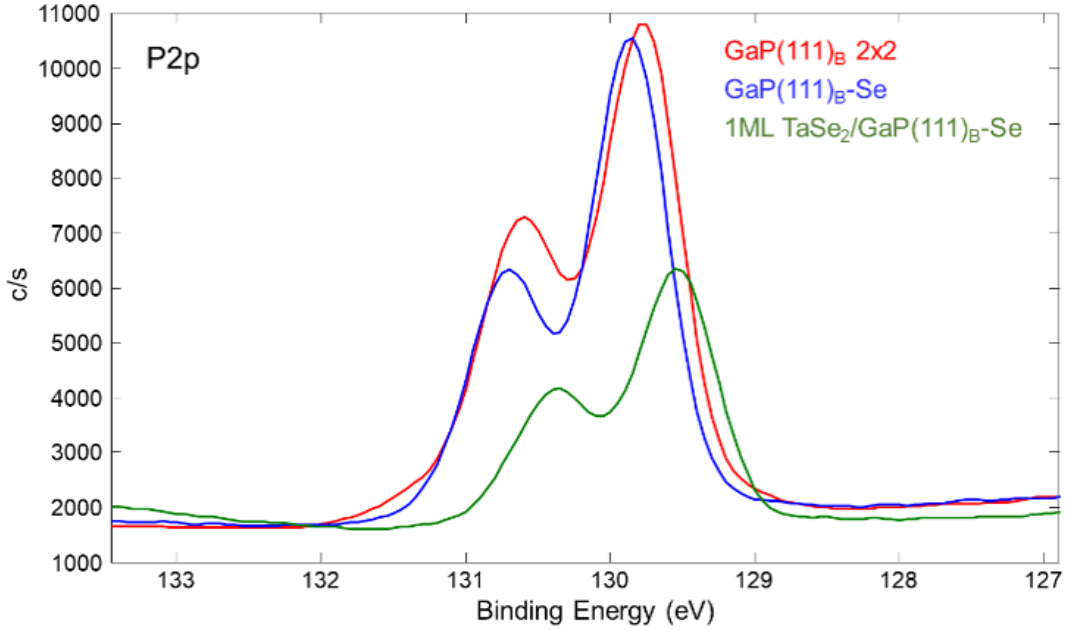

Figure S 6: Evolution of the binding energy of the P2p core level line from the deoxidized GaP(111)B 2×2 surface to the deposition of 1ML $TaSe_2$.

After selenium passivation, the P2p CL line BE increases a little bit to -129.87±0.025 eV, corresponding to a slight decrease of around 0.1 eV of the band bending (blue curve of figure S6). Finally, after 1 ML $TaSe_2$ deposition, the BE of the P2p CL decreases to -129.54 eV, leading to an increase of the band bending to 0.62 + 0.24 = 0.86±0.1 eV (green curve on figure S6).

The above values lead then to the relative position of the bottom of the conduction band at the GaP surface E_{cs} with respect to the Fermi level : $E_{cs} - E_f = 0.92 \pm 0.1$ eV. This is in good agreement with the depletion layer deduced from the STS measurements although there is a slight difference in the exact position of the bands with respect to the Fermi level.

Scanning Tunneling Spectroscopy

Spatially-resolved tunneling spectra were acquired across the SD pattern, as shown in Figure S7. The results obtained at different setpoint currents are shown Figure S8.

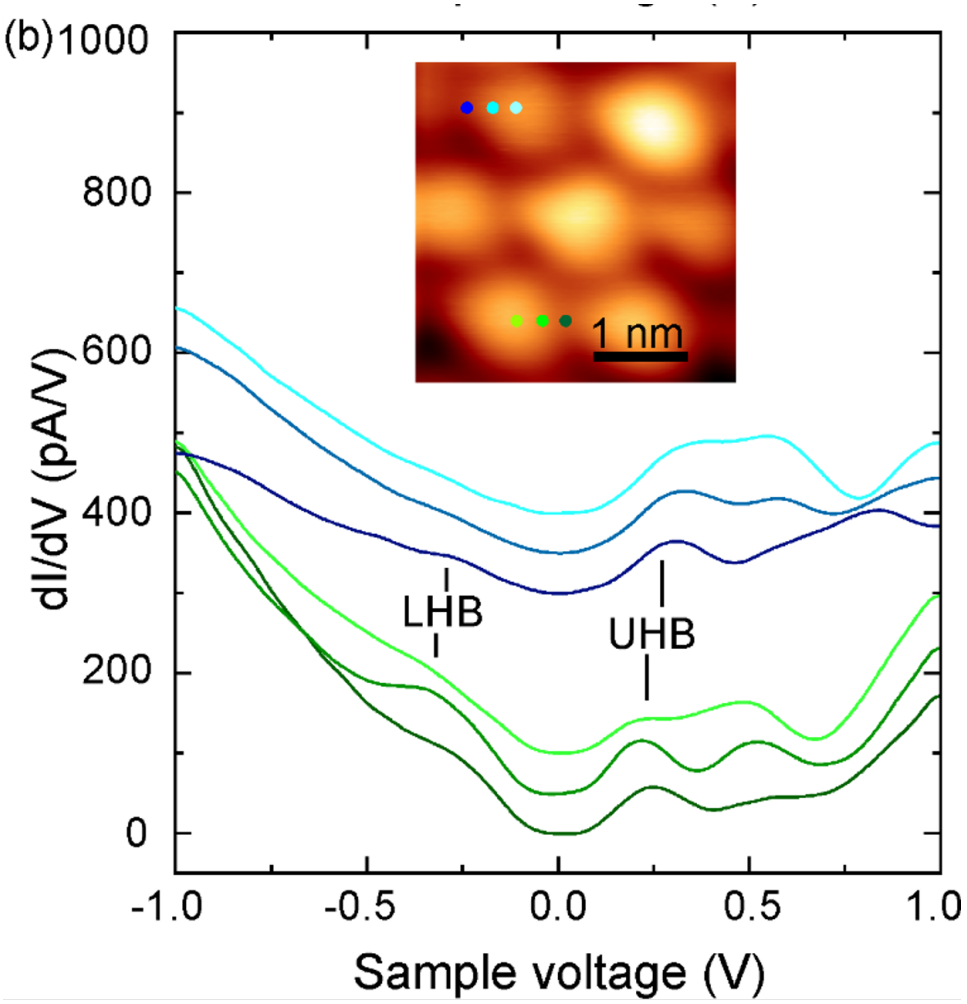

Figure S 7: (a) Differential conductance spectra measured across the SD pattern in the 1T-$TaSe_2$ epilayer at 77 K. Inset: the colored points in the STM image indicate the location corresponding to the spectra of the main figure. The curves have been offset for clarity. The energies of the UHB and LHB bands indicated in the Figure by vertical segments slightly shift due to potential fluctuation in the epilayer.

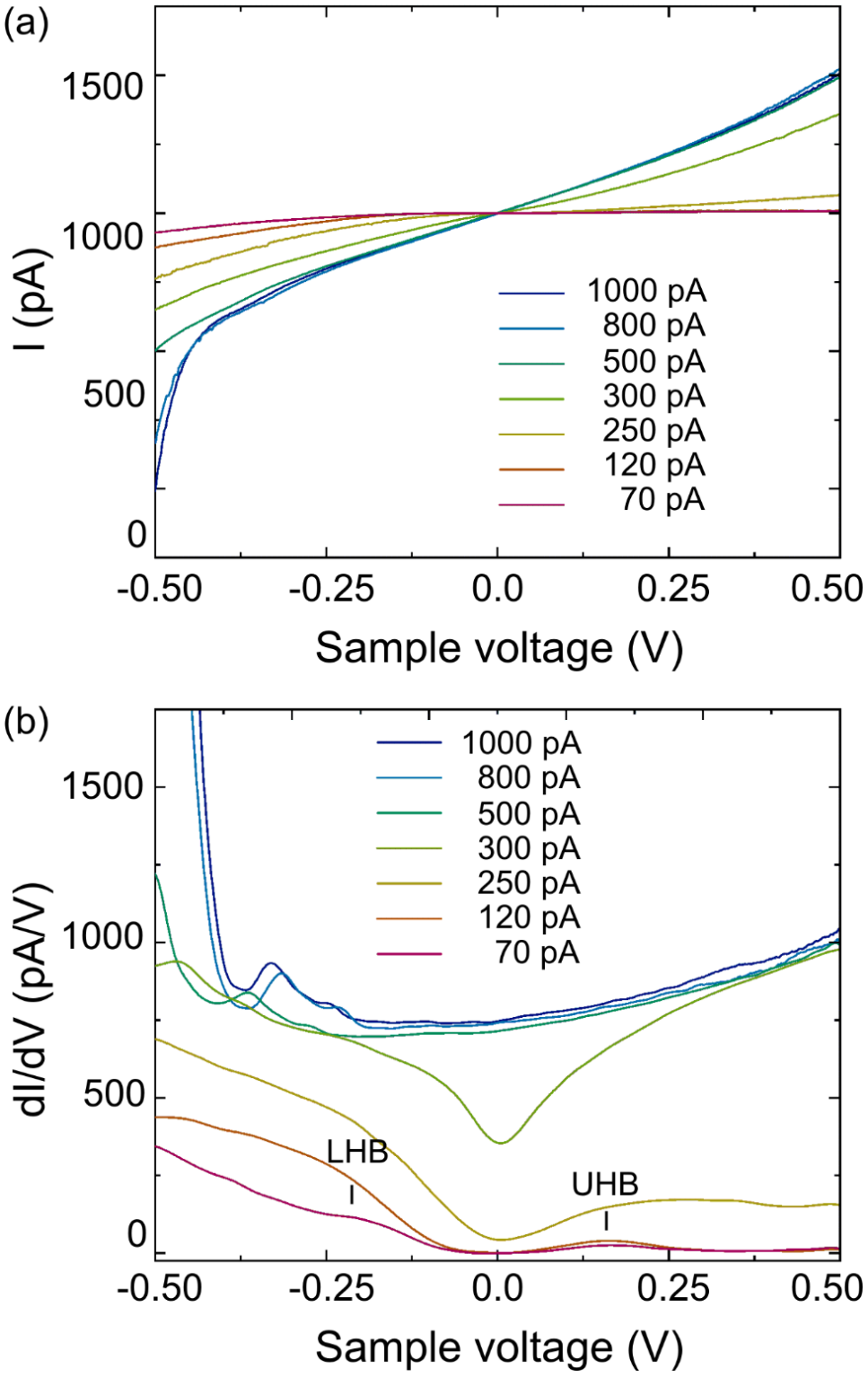

Figure S 8: Tunneling spectroscopy measured at different setpoint currents, corresponding to different tip-sample distances. (a) Current-voltage characteristics, (b) differential conductance characteristics measured with a lock-in amplifier using a 9 mV modulation at 471 Hz on the bias voltage.

Transport measurements in UHV

Four-point probe measurements of 1T-$TaSe_2$ monolayers grown on semi-insulating GaP substrates were performed with a multiple STM system under the supervision of a SEM in UHV with a base pressure lower than $5x10^{-10}$ mbar (Nanoprobe, Scienta Omicron). Prior to the experiments, the tungsten tips, obtained from electrochemical etching in NaOH, were thoroughly annealed in the UHV preparation chamber of the system to remove the thin oxide layer covering the tips and the Se cap protecting the $TaSe_2$ layer was sublimated. To measure the four-probe resistance of 1T-$TaSe_2$, the STM tips were first approached in the tunneling regime. The final approach was monitored with the tunneling current. Stable electrical contacts were obtained when the current saturated, yielding electrical resistances between two tips in the range 200-300 kΩ , higher than the measured 4P resistance of the epilayer of 11±2 kΩ.

Temperature dependent transport measurements

The transport measurements have been performed on $TaSe_2$ monolayers grown on insulating GaP(111)B substrates. The $TaSe_2$ monolayers are protected from oxidation with a 30 nm-thick Se capping layer. The samples are fixed at the extremity of a cryogenic insert designed for transport measurements mounted on a Janis VPF100 cryostat. The sample holder contains an insulating mounting surface and 4 fixed-position tungsten probes with limited range of movements for fine scale positioning. The design of the probes includes springs that allows good mechanical stability in electrical contact for a wide range of temperatures. All 4 probes are put in contact with the sample surface (Figure S9a) and the presence of the ohmic contacts is checked by measuring current-voltage characteristics between all pairs of probes at different temperatures ; typical results are shown Figure S9b. The resistance of a 130 nm-thick Se layer deposited on a GaAs insulating substrate was also measured as a function of temperature for comparison (black curve in Figure S9c). At high temperatures, the Se layer is at least 3 times more resistive than the $TaSe_2$ monolayer and becomes even more resistive

at lower temperatures. Therefore, the influence of the Se capping layer on the resistance behavior of the $TaSe_2$ monolayer is negligible over the whole measured temperature range.

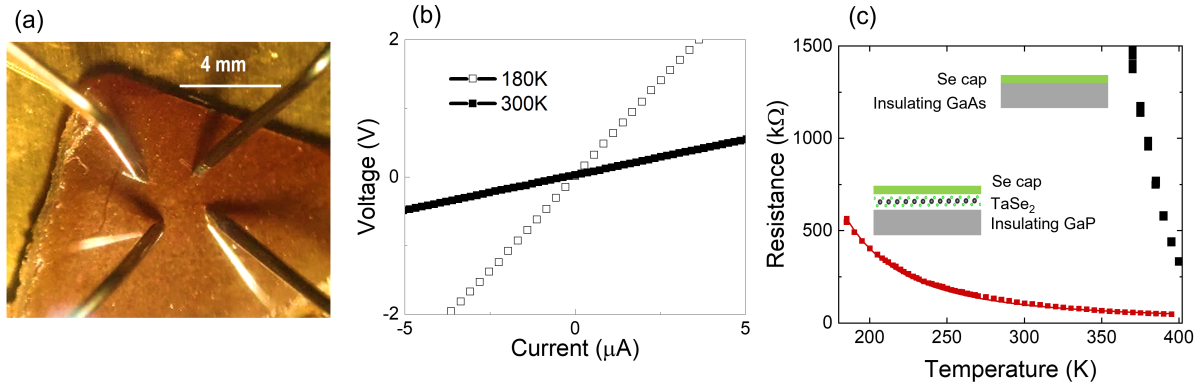

Figure S 9: (a) Optical image of the sample and electrodes. (b) Typical current-voltage characteristics measured between two probes, at the indicated temperatures. (c) Temperature dependence of the four-probes resistance measured in 1T-$TaSe_2$ monolayer capped with a 30 nm thick Se capping layer (red symbols) and in a sample with a Se cap only (black symbols). The insets illustrate the geometry of both with the Se cap plotted in green.

References

(1) Fairley, N.; Fernandez, V.; Richard-Plouet, M.; Guillot-Deudon, C.; Walton, J.; Smith, E.; Flahaut, D.; Greiner, M.; Biesinger, M.; Tougaard, S.; Morgan, D.; Baltrusaitis, J. Systematic and collaborative approach to problem solving using X-ray photoelectron spectroscopy. *Applied Surface Science Advances* **2021**, *5*, 100112.

(2) Moeini, B.; Linford, M. R.; Fairley, N.; Barlow, A.; Cumpson, P.; Morgan, D.; Fernandez, V.; Baltrusaitis, J. Definition of a new (Doniach-Sunjic-Shirley) peak shape for fitting asymmetric signals applied to reduced graphene oxide/graphene oxide XPS spectra. *Surface and Interface Analysis* **2022**, *54*, 67–77.

(3) Doniach, S.; Sunjic, M. Many-electron singularity in X-ray photoemission and X-ray line spectra from metals. *J. Phys. C: Solid State Phys.* **1970**, *3*, 285.

(4) Chiang, S.; Wertheim, G.; DiSalvo, F. Many-electron screening in narrow-band metals; XPS in layered dichalcogenides. *Solid State Communications* **1976**, *19*, 75–78.

(5) Hughes, H. P.; Scarfe, J. A. Site Specific Photohole Screening in a Charge Density Wave. *Phys. Rev. Lett.* **1995**, *74*, 3069–3072.

(6) Horiba, K.; Ono, K.; Oh, J. H.; Kihara, T.; Nakazono, S.; Oshima, M.; Shiino, O.; Yeom, H. W.; Kakizaki, A.; Aiura, Y. Charge-density wave and three-dimensional Fermi surface in \$1T\ensuremath{-}{\mathrm{TaSe}}_{2}\$ studied by photoemission spectroscopy. *Phys. Rev. B* **2002**, *66*, 073106.

(7) Geppert, I.; Eizenberg, M.; Ali, A.; Datta, S. Band offsets determination and interfacial chemical properties of the Al2O3/GaSb system. *Applied Physics Letters* **2010**, *97*, 162109.